REVIEW PAPER

Corrosion Resistance Behavior of GTAW Welded AISI type 304L Stainless Steel

Gopinath Shit[1,2] · M. V. Kuppusamy[3] · S. Ningshen[1,2]

Abstract Stainless steel (SS) has broad application in nuclear and several industries as structural material attributed to the desirable mechanical and suitable corrosion resistance properties. Corrosion resistance behaviors and microstructural evolutions of type 304L SS gas tungsten arc welded (GTAW) joint of different thickness were investigated using optical microscopy, scanning electron microscopy, X-ray diffraction, micro-Vickers hardness test and electrochemical techniques. Microscopic analsis reveals the weld microstrcture, interdendritic δ-ferrite of lathy and skeletal features along with austenite structure. Hardness is more in 6-mm-thick welded sample attributed to δ-ferrite contents. The measured corrosion rate in boiling HNO_3 increases with the increase in the thickness of the welded specimen, and base metal shows a marginally higher corrosion rate compared to weld metals. The corrosion rate of the base and weld metals of the AISI type 304L SS in 65% nitric acid is in the acceptable range. However, as the delta ferrite with a higher amount of chromium is present, the austenite matrix in the microstructure results in a lower corrosion rate of the weldment compared to its base material. The electrochemical corrosion behaviors of type 304L SS base metal and weldments in 6 M HNO_3 solution at 25 ± 1 °C are evaluated using potentiodynamic polarization and electrochemical impedance spectroscopy methods. The corrosion resistance, hardness and microstructure behavior of GTAW welded AISI type 304L SS are elaborated and discussed.

1 Introduction

Stainless steels (SSs) are extensively used in several industries such as nuclear industries, chemical industries, medical industries, oil and gas industries, offshore industries, etc., that require good corrosion resistance and mechanical strength [1, 2]. The corrosion resistance of stainless steel that contains more than 12% Cr is attributed to the formation of a thin and self-healing layer of chromium oxide film that provides resistance in the corrosive environment [3]. Among the austenitic stainless steel series, alloying elements such as N, Ni, Mn, Si and Mo are added along with controlled trace elements (B, S, P, etc.) for a specific requirement and its application in industries [1–4]. As an example, for highly corrosive nitric acid applications, controlled chemical composition and microstructure, low-carbon and restricted levels of C, Si, P, S and Mo are required to achieve consistently a good intergranular corrosion resistance in nitric acid. The resultant alloy steels also called as a nitric acid grade SS are characterized by the controlled chemical composition of alloying elements, the microstructure that minimizes intergranular corrosion sites, and further additions of Si and

✉ Gopinath Shit
gopims@igcar.gov.in

1 Homi Bhaba National Institute, Mumbai 400 094, India

2 Corrosion Science and Technology Division, Metallurgy and Materials Group, Indira Gandhi Centre for Atomic Research, Kalpakkam 603102, India

3 Quality Assurance Division, Indira Gandhi Centre for Atomic Research, Kalpakkam 603102, India

higher Cr contents that enhance the transpassive corrosion or dissolution [3–5]. However, the trace amount of C is always present in the steel either being intentionally added or as an impurity. The deleterious effects of carbon impurity to corrosion resistance can be lower by adding carbide stabilizer such as titanium, niobium and tantalum to minimize the formation of chromium carbide [6].

Welding is a widely used joining process for fabrication of stainless steel structure, and it is used as an alternative to the riveting process [7]. The process of welding has been widely used in joining of pipes [7], industrial components/equipment [8, 9] and fabrication of structural material in chemical, space and nuclear component [10–12]. However, the welding processes are strongly influenced by the materials properties such as microstructure [13–18], mechanical behavior [14–19] and corrosion resistance [4, 20]. The influences of welding on material properties are attributed to the micro-segregation of chromium carbide at the grain boundaries through the sensitized process, formation of secondary phases ($\gamma \rightarrow \delta$ and σ transformation during cooling) and resultant crack or porosity during welding [21, 22]. Moreover, the formation of secondary phases (δ-ferrite) plays a significant role in the welding material properties determination. The δ-ferrite content not only affects the corrosion resistance but also improves the ductility and toughness in SS. Therefore, about 5–10% delta ferrite content in stainless steel weldments are maintained to minimize solidification and hot cracking and improve strength and corrosion resistance [23, 24]. Moreover, higher δ-ferrite (10 vol. %) is known to decrease the hot workability [4]. Therefore, controlled δ-ferrite content during welding of austenitic stainless steels is essential to minimize solidification and hot cracking. Many factors that generally influence the weld microstructure in the stainless steel are heat input, welding speed, welding power and rate of cooling, number of passes, etc. [4–22]. The effect of heat input has important role in the secondary austenite (γ') phase formation in duplex stainless steel, and it affects the corrosion resistance of the weldment [25]. Atamert et al. [26] have shown that high heat input can increase corrosion resistance by partitioning the chromium and Mo into the ferrite phase with decreasing temperature in duplex stainless steel (DSS). In austenite SS with an increase in heat input, the percentage of delta ferrite increases in the HAZ, whereas delta ferrite percentage decreases in the weld metal region that can influence the passivity and corrosion resistance [27].

There are many welding processes for different industrial applications that include shielded metal arc welding (SMAW) under low thermal heat condition with 5% ferrite in the welded zone showing improved mechanical properties [20, 28], and with the decrease in the test temperature, fatigue crack growth of the base metal decreases for 304 SS pipe line [20, 29]. Similarly, laser-induced welding processes (laser and laser-TIG), have several advantages over conventional welding (TIG) with respect to faster cooling rate, localized heating, deep penetrating, narrow welds (high depth-to-width ratios), higher melting efficiency, less heat-affected zone (HAZ), ease of access to the weld, seam through fiber delivery, facilitating the welding with intricate geometries, lower defect and improved mechanical properties [29, 30]. Increase in hydrogen content introduced during welding increases the penetration depth [31] and the weld shape changes from wide shallow to narrow deep by the addition of oxygen [32]. The chromium equivalent (Cr_{eq})-to-nickel equivalent (Ni_{eq}) ratio in the range of 1.52–1.9 is desirable to control solidification in type 304L SS [32, 33], and ∼ 3 to 20% ferrite content is desirable to eliminate flaws and hot cracking [18]. Among the various welding methods, gas tungsten arc welding (GTAW) is one of the most widely used. It is also a reliable method for welding stainless steels. Besides, it has several advantages such as, easy to process, cleanliness, ease in welding complicated shapes with large and small dimensions, applicable to a wide range of materials and also [4] inexpensive [11, 18]. The main aim of the present investigation is to study the effects of different weld thicknesses of type 304L stainless steel and correlate the microstructural aspects with the corrosion resistance and hardness behavior.

## 2 Experimental Details

2.1 Materials

The chemical composition of the base materials of 3-mm- and 6-mm-thick plate of AISI type 304L SS used for the present work is shown in Table 1a. The AISI type 308L SS solid electrode of 1.6 mm and 2.0 mm diameter were selected as filler material for the welding process. The chemical composition of both the base and filler wire is given in Table 1(a and b).

2.2 Welding Process

AISI type 304L SS plates were butt-jointed using AISI 308L SS filler rod in different conditions by GTAW welding process. Schematic diagrams of the weldment specimen preparation are shown in Fig. 1. It involved six passes for 6-mm-thick and two passes for 3-mm-thick specimens, where the shielding gas was 99.99% commercial argon, and root gap of the base metal was maintained between 2 and 2.5 mm, and inter-pass temperature was maintained within 120 °C. Welding parameters are listed in Table 2a, b. Before the welding process, all the sheets

Table 1 Chemical composition of (a) type 304L stainless steel base metal and (b) 308L filler rod

Elements	Cr	Ni	C	Si	Mo	P	Co	Ti	Mn	Fe
(a) Type 304L stainless steel base metal										
Wt%	18.2	9.2	0.02	0.32	0.05	0.03			0.59	Balance

Elements		Cr		Ni		Mn		Mo		C
(b) 308L filler rod										
Wt%		18.1		10.3		1.6		< 0.04		0.017
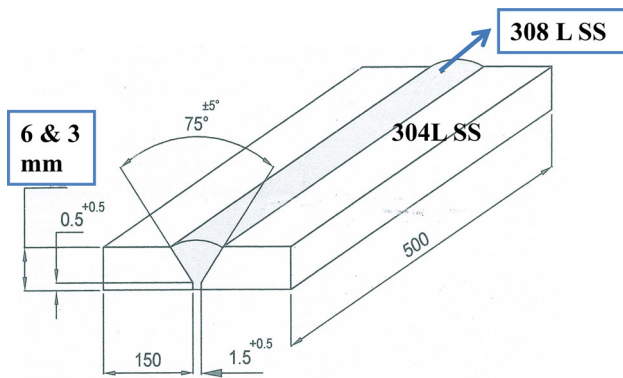
Fig. 1 Schematic of butt joint GTAW process

were cleaned mechanically and chemically by acetone in order to remove any source of contamination like rust, dust, oil, etc. No preheat or post-heat treatment was carried out on the specimens after the welding process [4]. During and after welding, joints were visually inspected for their quality, and it was ensured that all weld beads possessed good geometrical consistency and were free from visual defects like surface porosity, blow holes, etc. [4]. In addition, 99.99% pure Ar was used as shielding gas to avoid the contamination of other gases like N_2, O_2 and H_2 with the welded zone.

2.3 Microstructure Analysis

The cross section of the test specimens was mechanically ground with SiC emery paper and finished up to the diamond grade of 1 μm finish. An etching solution of nitric acid with ethyl alcohol (Nital) was used. The microstructures were analyzed by using OM and SEM model of Camscan 3200 with photomultiplier tube (PMT) detector. XRD of model INEL X-ray diffractometer 2000 (France) with CoKα (wavelength (λ) = 0.178897 nm) X-ray source was used for identification of the phases present in the welded zone of the sample. Vickers hardness measurement was taken using FIE Vickers Hardness instrument (India, Model VM-50), with a load capacity of 10 kgf for 15 s.

Ferrite number was measured using the nondestructive technique with the Fischer Feritscope FMP30 to measure the ferrite content. This measurement was taken at the center of the welded zone.

2.4 Corrosion Resistance Evaluation—Huey Test

The corrosion resistance of the AISI type 304L SS was evaluated using ASTM A262 standard practice-C (Huey test) [34]. The experiments were conducted by immersing the test coupon for five times with an interval of 48-h

Table 2 Welding parameters for (a) 6-mm-thick specimen and (b) 3-mm-thick specimen

S.I. no	Passes	Current (A)	Voltage (V)	Speed (mm/S)	Heat input (J/mm)
(a) 6-mm-thick specimen					
1	Root	60	8	0.625	768
2	Intermediate	75	9	1.196	671
3	3rd pass	90	10	1.096	821
4	4th pass	90	10	1.087	828
5	5th pass	90	10	1.563	576
6	Final	90	10	1.894	475
(b) 3-mm-thick specimen					
1	Root	70	9	0.992	670
2	Final	80	10	1.1	727

periods (240 h) in the boiling 65% nitric acid. The nitric acid solution was renewed after the interval of every 48 h in order to avoid the accumulation of corrosion products which could increase the corrosion rate of the specimens in the boiling liquid phase [35]. Subsequently, the specimens were rinsed after the completion of the test in distilled water, cleaned with acetone and dried in hot air, and the average corrosion rate for the specimens was calculated using the equation describe [36].

$$\text{Corrosion rate} = \frac{K \times W}{ATD}$$

where $K = (3.45 \times 10^6$ for mpy and 8.76×10^4 for mm/yr); T = time of exposure in hours; A = area in cm^2; W = mass loss in gms and D = density in gm/cm^3.

## 2.5 Electrochemical Corrosion Measurements

The electrochemical corrosion experiments were carried out using a three-electrode system. The test specimen was used as the working electrode, saturated Ag/AgCl as the reference electrode and Pt as the counter electrode. After stabilization of the system potential, the OCP measurements were recorded up to 60 min. All potentiodynamic polarization experiments were performed at the scan rate of 10 mV/min, and potentiodynamic anodic polarization experiment was carried out till it reached transpassive potential region [37]. All the electrochemical experiments were carried out at room temperature (25 ± 1 °C), and two to three sets of tests were conducted for each specimen, and the experiments showed almost reproducible results.

Electrochemical impedance spectroscopic (EIS) measurements were taken under open circuit potential condition using Solartron 1255 frequency response analyzer and Solartron 1287 electrochemical interface [38]. The EIS experiments were performed in the frequency range of 10^6–0.01 Hz by superimposing an AC voltage of 10 mV amplitude, and the data were recorded at 10 points per decade. The impedance responses obtained from the Nyquist plots were analyzed by Z-View software using a simple equivalent circuit model (R_s. (R_p∥CPE)) [39], shown in Fig. 2; R_s is the solution resistance, R_p is the polarization resistance, and CPE is the constant phase element. CPE represents the generalized form of passive film double-layer capacitance, and it is used for obtaining the fit values of the experimental data.

A typical expression for CPE is represented as [39–41]:

$$Z_{\text{CPE}} = 1/[C(j\omega)^n] \tag{1}$$

where ω is the angular frequency, C and n are the frequency-independent fit parameters; $J = (-1)^{1/2}$ and $\omega = 2\pi f$, where f is the frequency in Hz. The adjustable fit parameter $n = 1 - 2\alpha/180$, ranges between 0.5 and 1, and α
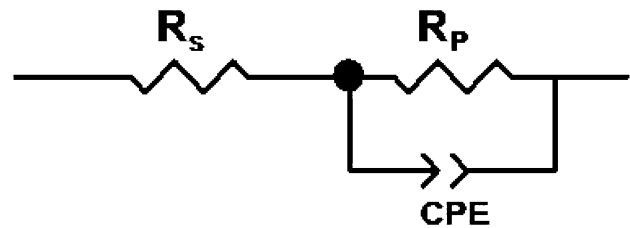

Fig. 2 Equivalent circuit model for fitting impedance data (using Z-view software)

is a measure of the depression angle in degree that evaluates the semicircle deformation/depression. When the value of $n = 1$, the fitted equivalent circuit is for a capacitor, and when $n = 0.5$, CPE describes the Warburg impedance [42].

3 Results and Discussion

3.1 Microstructure Features of Welded Type 304L Stainless Steel

In Fig. 3, XRD analysis reveals that the γ-austenite and δ-ferrite phases are present in the welded zone. After welding and during the cooling process, δ to γ transformation occurs in the fusion zone. In GTAW process, since it is diffusion-controlled transformation, delta ferrite is retained in the welded zone and helps to resist against the microfissuring and hot cracking during solidification [43]. This can also result due to the peritectic–eutectic transformation which takes place at the end of the solidification process; when metal cools through the two-phase delta ferrite and austenite field, diffusion-controlled reaction can take place by which austenite transforms into ferrite [44]. A small amount of delta ferrite is necessary to prevent hot cracking in the weldment and fully austenite phase in the weld
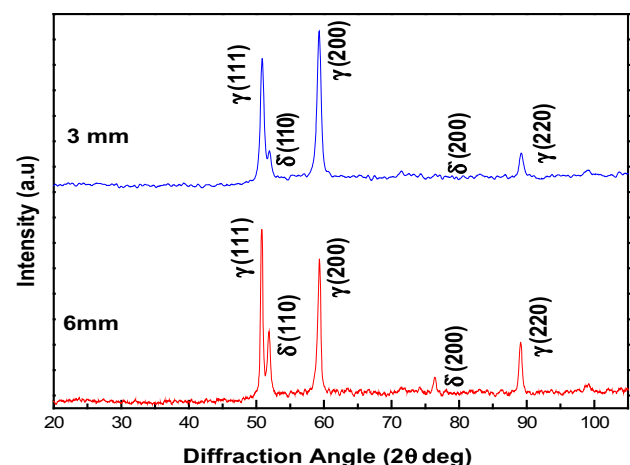
Fig. 3 XRD pattern of the welded zone

deposit is susceptible to micro-fissuring during solidification [41].

The solidification or cooling rate of a weldment can be calculated by the following way [30, 45–49]:

Thickness of the plate (h): 3 mm or 6 mm
Heat input (H_{net}): q/v = heat or energy/welding speed
Initial plate temperature (T_o): Room temperature (RT)
Temperature of interest at which cooling rate is desired (T_i): 1500 °C
Specific heat (C): 502.42 J/kg K
Density (ρ): 8000 kg/m^3
Relative plate thickness (τ): $h\left[\rho C(T_i - T_o)/H_{net}\right]^{1/2}$

When relative plate thickness is $\tau < 0.6$, in thin plate, the cooling rate equation is used, and similarly in thick plate cooling rate equation is used when $\tau > 0.9$.

If the value of τ is in the range of 0.6–0.9, then the value 0.75 is used to decide which cooling rate equation should be used.

Cooling rate (R) equation for thin plates:

$$\left[2\pi\kappa\rho C(h/H_{net})(T_i - T_o)^3\right]^o \text{C/sec} \tag{2}$$

Cooling rate (R) equation for thick plates:

$$\frac{\{2\pi\kappa(T_i - T_o)\}}{H_{net}} \text{C/sec} \tag{3}$$

So, for a particular material, heat input (H_{net}) is the important parameter for the determination of cooling rate.

The typical optical microscopic and SEM images of the welded zone with different magnifications are shown in Fig. 4 that shows the dendritic structure of the weld zone which at higher magnification provides the information about the dendrite phase and interdendritic phase. The dendrite phase probably arises from δ-ferrite (Cr-rich) phase of steel and the interdendritic phase due to the austenite (Ni-rich) phase of steel [21, 22]. This can be predicted from the XRD analysis also. The interdendritic phase appears brighter in comparison to dendrite phase in SEM images due to the high Ni content in the interdendritic phase.

The variation of the delta ferrite morphology in the fusion/welded zone is shown in Fig. 5. It is evident that two different delta ferrite features are formed within the austenite matrix of the welded zone, one in the form of skeletal ferrite and other a lathy delta ferrite. Similar features of delta ferrite formations are known to form in GTAW welded specimen. The variation of delta ferrite in the weld zone appears due to the variation of thermal cycles and cooling rates of the weld zone [4, 50, 51]. These differences in the cooling rate in the weld zone are the reason for the change in the morphology during ferrite transformation. The delta ferrite predominantly contains the skeletal ferrite for 3-mm-thick weldment, whereas it is lathy delta ferrite morphology for 6-mm-thick weldment. This can be explained by the restricted diffusion during ferrite and austenite transformation, which is attributed to the high cooling rate for the formation of lathy ferrite. When the cooling rate is low, the austenite consumes the ferrite until it gets saturated with ferrite promoting elements like (Cr, Mo, etc.) and gets depleted in austenite promoting element (Ni, C, N, etc.) which is stable at a lower temperature with limited diffusion [52].

In Fig. 6, the optical micrographs of the HAZ, fusion zone and welded zone are represented. This microstructure shows that the dendritic arm spacing in the welded zone at the HAZ increases with less number of the pass during welding. The number of passes for 6-mm-thick welded sample is higher in comparison with the 3-mm-thick sample, resulting in larger grain size for 3-mm-thick specimen than that of 6-mm-thick sample. This can be attributed to the thermal cycling and recrystallization occurring during multipass welding, that resulted in epitaxial grain growth. Such growth is beneficial against the concentration of stresses at the weld zone-HAZ interface. The mechanism behind such growth is related to the crystal structure and chemical composition at weld zone and base metal [4, 53].

The measured ferrite numbers of 6-mm-thick and 3-mm-thick welded specimens are 8.7 and 5.7, respectively. The variation of delta ferrite content may be attributed to the variation of thermal cycling and cooling rates by increasing the number of passes. The delta (δ) to gamma (γ) transformation is a diffusion-controlled process; high cooling rate does not permit sufficient time for such transformation [4]. This results in a higher amount of delta ferrite inside the austenite matrix of the welded zone. It is desirable that 5–10% delta ferrite are retained in the austenite matrix of the welded zone to prevent the hot cracking and solidification and also to improve the ductility and corrosion resistance of the welded joint properties. Hence, the determination of ferrite content is very important. By determining the ferrite number at different places of the welded zone, it can be concluded that all these specimens are in secure range.

3.2 Hardness Results of Base and Weld Type 304L Stainless Steel

Hardness of the welded samples was measured in the longitudinal direction parallel towards the base plate surface [54]. Figure 7 shows the plot of Vickers hardness versus distance from the welded zone for 6-mm-thick and 3-mm-thick 304L stainless steel specimens. The hardness profile of the sample shows that the welded zone indicates minimum hardness value for each specimen. This is because of the heat from the process in the weld zone
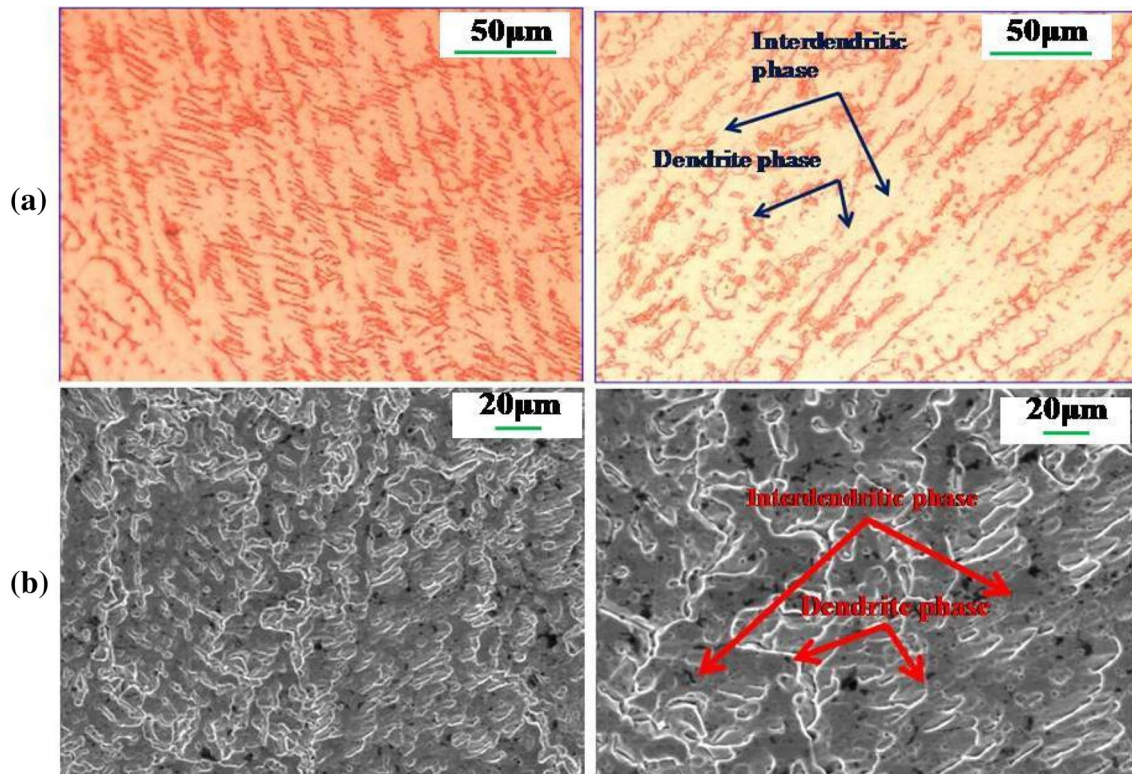
Fig. 4 The optical microscopy (**a**) and SEM (**b**) images of the weld zone, where dendrite structure and different phases present in the welded zone are indicated
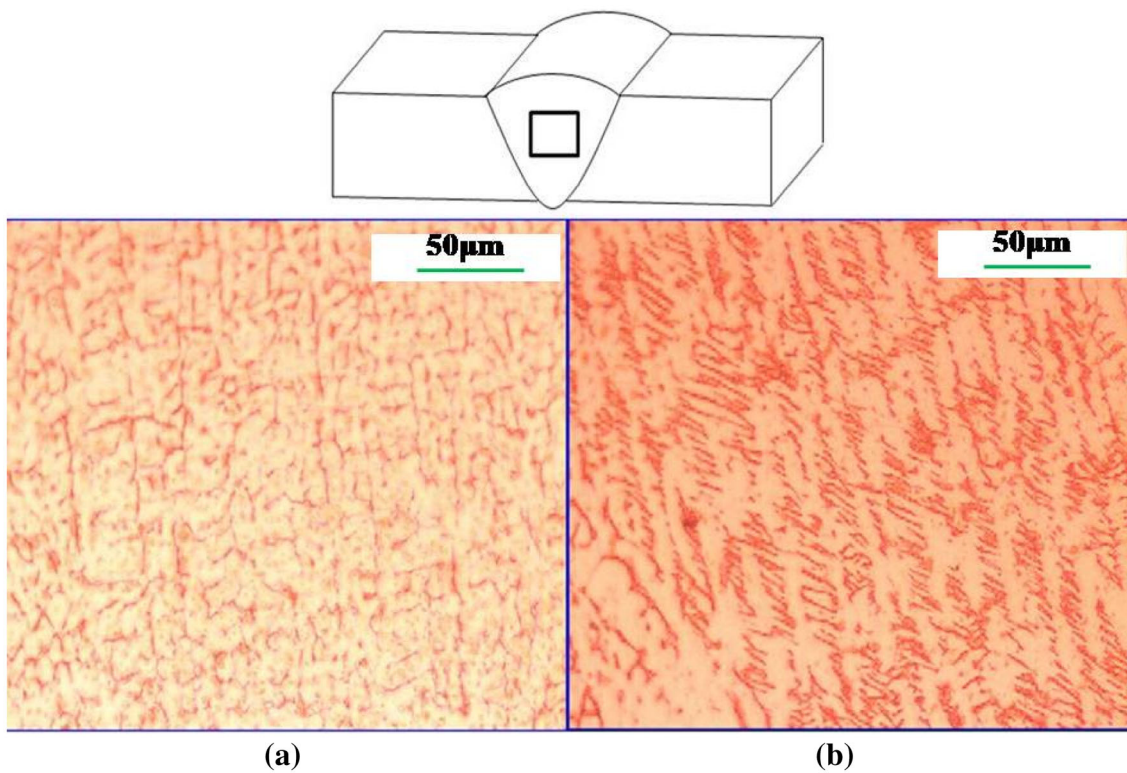
Fig. 5 Optical microscopy images of the weld zone: **a** skeletal ferrite morphology (3 mm), **b** lathy delta ferrite morphology (6 mm)
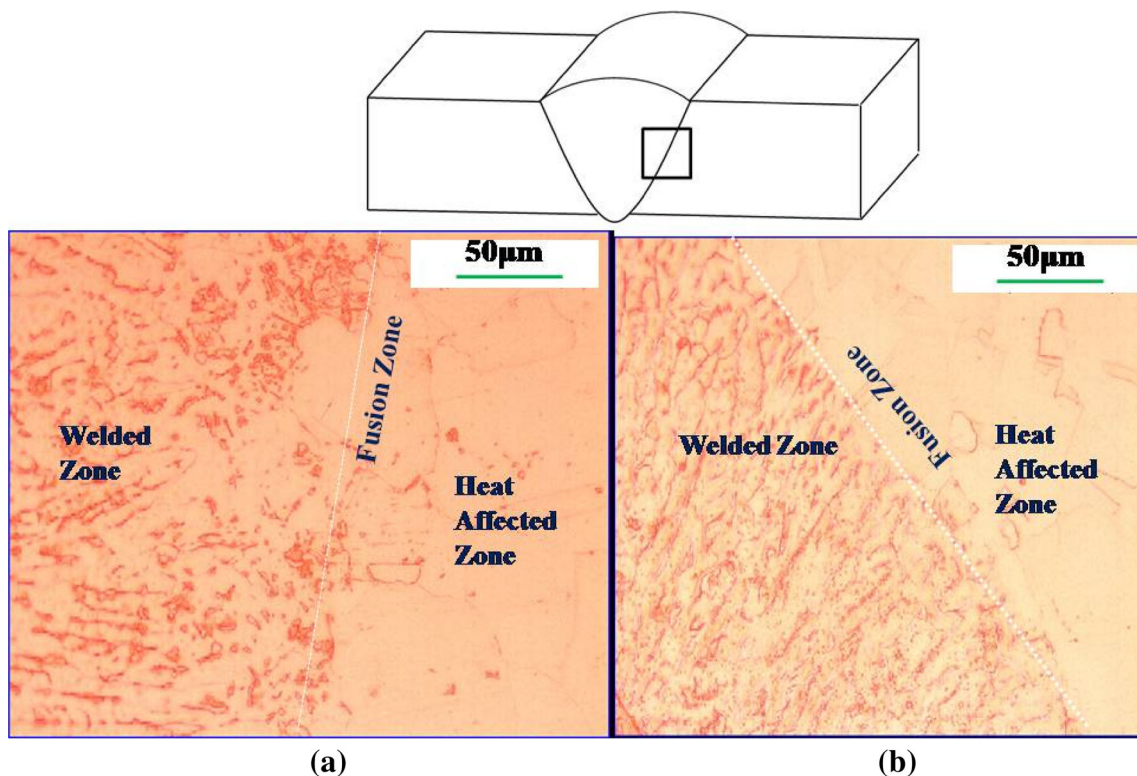
Fig. 6 Different zone of the weldment sample: **a** 6-mm-thick and **b** 3-mm-thick weld metal
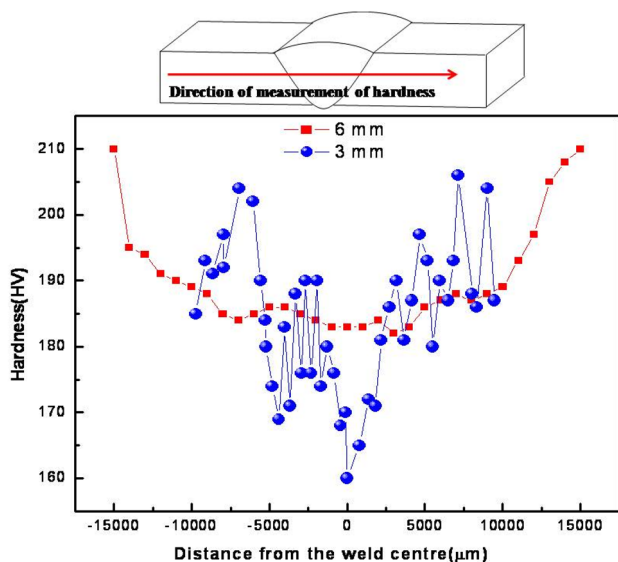

Fig. 7 Vickers hardness measurement of GTAW welded 3-mm-thick and 6-mm-thick specimens of type 304L stainless steel

causes annealing and recovery to take place that leads to drop in hardness. The hardness value gradually increases in the HAZ from fusion line to base metal. The increase in hardness near the HAZ is attributed to the slow cooling rate near the fusion line and subsequent grain growth [1, 4, 14]. Subsequently, the higher cooling rates near to the base

metal results in a finer grain and also the chemical and microstrctural homogeneity. The differences between 6-mm-thick and 3-mm-thick 304L stainless steel specimens with respect to hardness in the weld zone and heat-affected zone (HAZ) are evident. The hardness value is higher in the weld zone and HAZ for 6-mm-thick sample than 3-mm weld. This is attributed to the higher percentage of formation of δ-ferrite precipitate which impede the dislocation from occurring [55] and results in increase in the mechanical strength and coarse grain for 6-mm weld sample at weld and heat-affected zones, respectively [16, 51]. Musa et al. [56] explained that cooling rate is inversely proportional to heat input, resulting in a high cooling rate that leads to an increase in hardness value [57]. Therefore, the heat input value for final pass for 6-mm-thick SS material is ∼ 475 J/mm, whereas it is ∼ 727 J/mm for 3-mm-thick material. This results in higher hardness value of HAZ for 6-mm-thick SS material. In comparison, base metal shows the highest hardness value due to more chemical and microstructural homogeneity [4].

### 3.3 ASTM A-262 Practice-C Test (Huey Test) for Measuring Corrosion Rate

ASTM A-262 practice-C test (Huey test) has been performed in 65% boiling nitric acid medium for 240 h [3].

The corrosion rate has been measured by the weight loss measurement method and also to evaluate the susceptibility to IGC resistance. Figure 8 describes the plot of corrosion rate in mm/yr and mpy after each 48-h interval for 240-h exposure. For 6-mm-thick base metal of AISI type 304L SS, the obtained corrosion rate is 7.17, 6.72, 7.84, 16.9 and 18.5 mpy (or 0.88, 0.083, 0.097, 0.21 and 0.23 mm/yr). Similarly for 6-mm weld, 3-mm weld and 3-mm base metal, the measured corrosion rates are 3.75, 8.81, 12.63, 12.52 and 12.83 mpy (or 0.05, 0.13, 0.19, 0.19 and 0.19 mm/yr), 8.32 (0.089), 8.06 (0.086), 7.88 (0.084), 8.06 (0.086), 8.26 (0.088) and 4.72, 8.07, 8.15, 8.11, 8.31 mpy (or 0.08, 0.14, 0.14, 0.14, 0.14 and 0.14 mm/yr), respectively.

Figure 9 shows the plot of average corrosion rate of the base and weldment specimens. The measured corrosion rate of 6-mm-thick base material is 11.42 mpy or 0.29 mm/yr which is higher than that of 3-mm-thick base material of 8.26 mpy or 0.21 mm/yr. This may be attributed to the
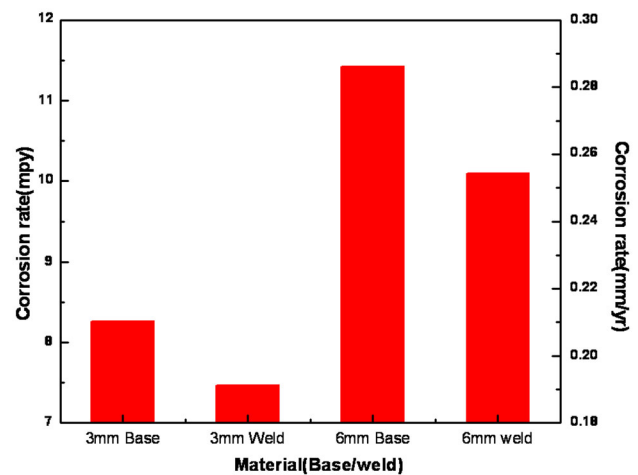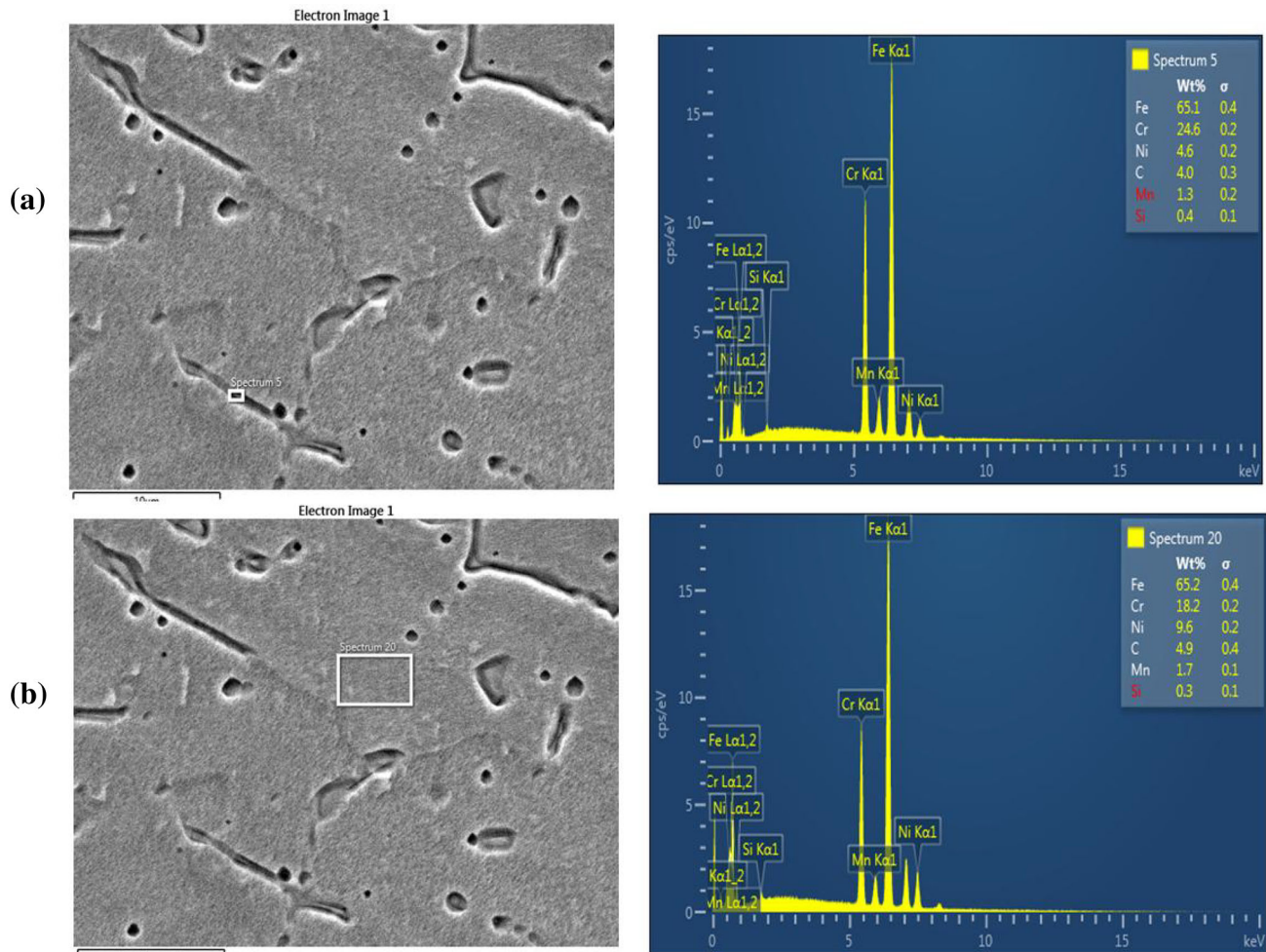
Fig. 9 Average corrosion rate comparison between base and weld metal of type 304L stainless steel

(a)

(b)

(c)

(d)
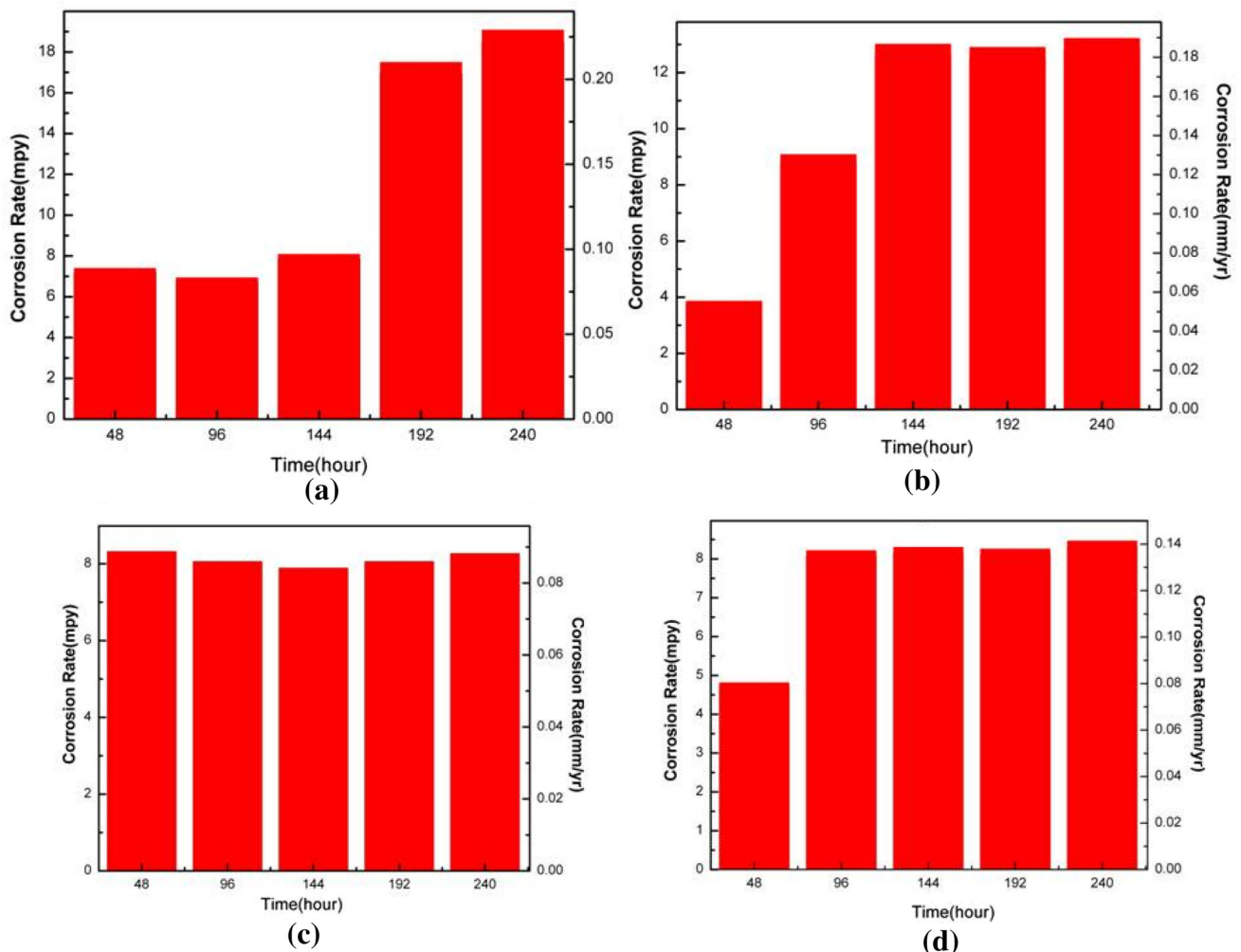
Fig. 8 Corrosion rate obtained after immersion in boiling nitric acid as per ASTM A-262 practice-C (Huey test) **a** 6-mm base metal, **b** 6-mm weld, **c** 3-mm weld and **d** 3-mm base metal of type 304L stainless steel

Fig. 10 EDS elemental composition of type 304L SS weldments analysis at **a** at δ-ferrite region (Cr $\sim$ 24.6; Ni $\sim$ 4.6 wt%) **b** at austenite region (Cr $\sim$ 18.2; Ni $\sim$ 9.6 wt%)

reduction in thickness affected by rolling of the samples. Grain size generally decreases with an increase in the percentage of rolling, and the rolling may also affect the desensitization process [52]. Schino et al. [58] reported that corrosion rate decreases with the decrease in grain size, as the IGC is caused by the volume fraction of the precipitation of carbide at grain boundary, and corrosion rate decreases with increasing of grain boundary area per unit volume and resulted in decrease in chromium depletion for a given carbon content affecting the corrosion resistance.

On the other hand, the corrosion rate of the weldment material of 6-mm and 3-mm samples are 10.1 mpy or 0.26 mm/yr and 7.47 mpy or 0.19 mm/yr, respectively; the measured corrosion rate of weldments is marginally lower than that of its base counterpart. As the delta ferrite contains higher amount of chromium, the austenite matrix in the microstructure results in lower corrosion rate of the weldment compared to its base material [4, 23]. Similarly, EDS results of chromium in the delta ferrite and austenite matrix that support this are shown in Fig. 10. It is proposed

that the redistribution or removal of MnS inclusion which acts as the preferred site for corrosion initiation [4] also improve corrosion resistance in the welded material. It is well known that corrosion resistance in austenitic SS is derived from the formation of a tenacious and self-healing thin passive oxide film that develops on the surface when exposed to a highly oxidizing environment such as nitric acid. It is evident that, despite the test being conducted in a highly oxidizing and boiling 65% (wt%) nitric acid medium, the measured corrosion rates of the base and its weld metals (0.19–0.23 mm/y) are in the lower and acceptable range. However, the surface morphology after the boiling test of 240 h shows an IGC attack in both type 304L SS base and weld metals (3 and 6 mm) with a significant preferential attack along grain boundaries, thereby indicating IGC attack (Fig. 11). In austenitic SS for aqueous spent fuel reprocessing applications, corrosion problems have been experienced with the type 304L SS materials due to knife line attack at weld regions and end grain attack at pipe cut sections [3, 5, 7]. Such corrosion
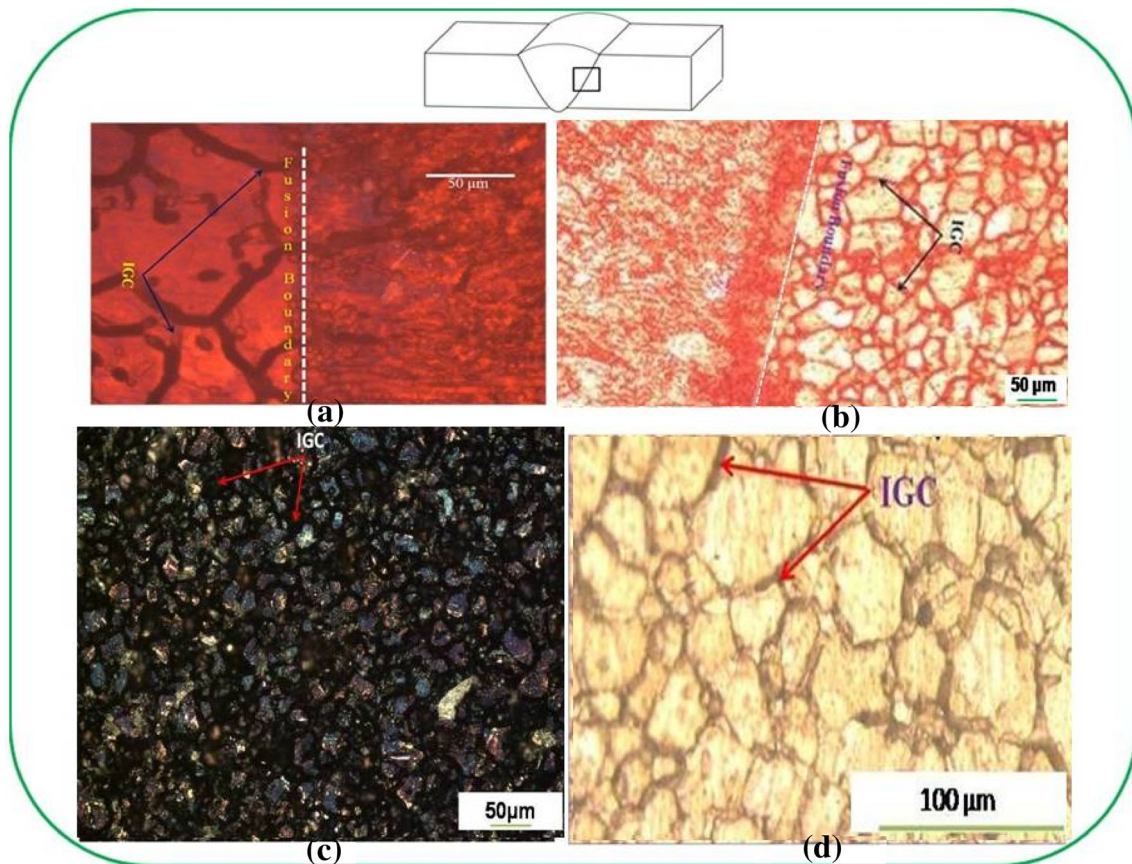
Fig. 11 Microstructures of corrosion-tested specimens of type 304L stainless steel samples: **a** 6-mm-thick welded; **b** 3-mm-thick welded; **c** 6-mm-thick base metal and **d** 3-mm-thick base metal, after boiling in 65% nitric acid for 240 h

attacks along the grain boundaries in type 304L SS lead to the grain dropping during the propagation of the corrosion. Furthermore, in any critical application for use in nitric acid service, the stainless steels and its alloy materials must exhibit less than 18 mpy (0.45 mm/y) in the sensitized condition, which occurs during welding and heat treatment process [3]. The above results show that the observed corrosion behavior of type 304L SS in boiling liquid nitric acid is interplay of different factors like nature of the passive film, dissolved ions, temperature, etc. [59]. The corresponding microstructure is shown in Fig. 10, and the microstructures indicate that in the nitric acid environment, sever intergranular corrosion (IGC) attack along the grain boundaries are observed. However, the open grooves at grain boundaries are not visible.

In the boiling liquid phase, the corrosion rate of type 304L SS (3 mm) remains relatively low, at the end of the 240-h test and the corrosion rate of type 304L SS (3 mm) is much lower compared to type 304L SS (6 mm thick). In the boiling liquid phase, the corrosion rate is also dependent on the oxidizing ions (i.e., Fe^{3+}, Cr^{3+}, Ni^{2+}, etc.) generated during the corrosion reaction in the liquid

solution [5, 35]. Further, corrosion is known to accelerate in the presence of these oxidizing ions [42] in highly oxidizing and boiling nitric acid solutions during immersion experiments; such a condition favors and leads to gradual shift in the corrosion potential to the transpassive state, thereby accelerating the corrosion reaction [60]. It is evident that the generations of such oxidizing ions of chromic and ferric ions influence the corrosion resistance of stainless steels in nitric acid [5], resulting in IGC attack. In general, the corrosion of austenitic stainless steels in nitric acid in the highly oxidizing liquid solution can lead to intergranular attack even in non-sensitized steels [35]. The higher corrosion rate in a thicker plate of the type 304L SS (6 mm) may also be attributed to the etching of the specimen and also severe corrosion is specific for the thicker plate [35]. For the austenitic type 304L SS in the nitric acid medium, the enhanced and preferential IGC attack at grain boundaries is observed largely due to segregation of impurities, such as Si, P, C, Mo, N, etc., and local depletion and precipitations of chromium-rich chromium carbides ($Cr_{23}C_6$) phases (sensitization in heat-affected zone). The higher corrosion rate in AISI type 304L SS (6 mm) may
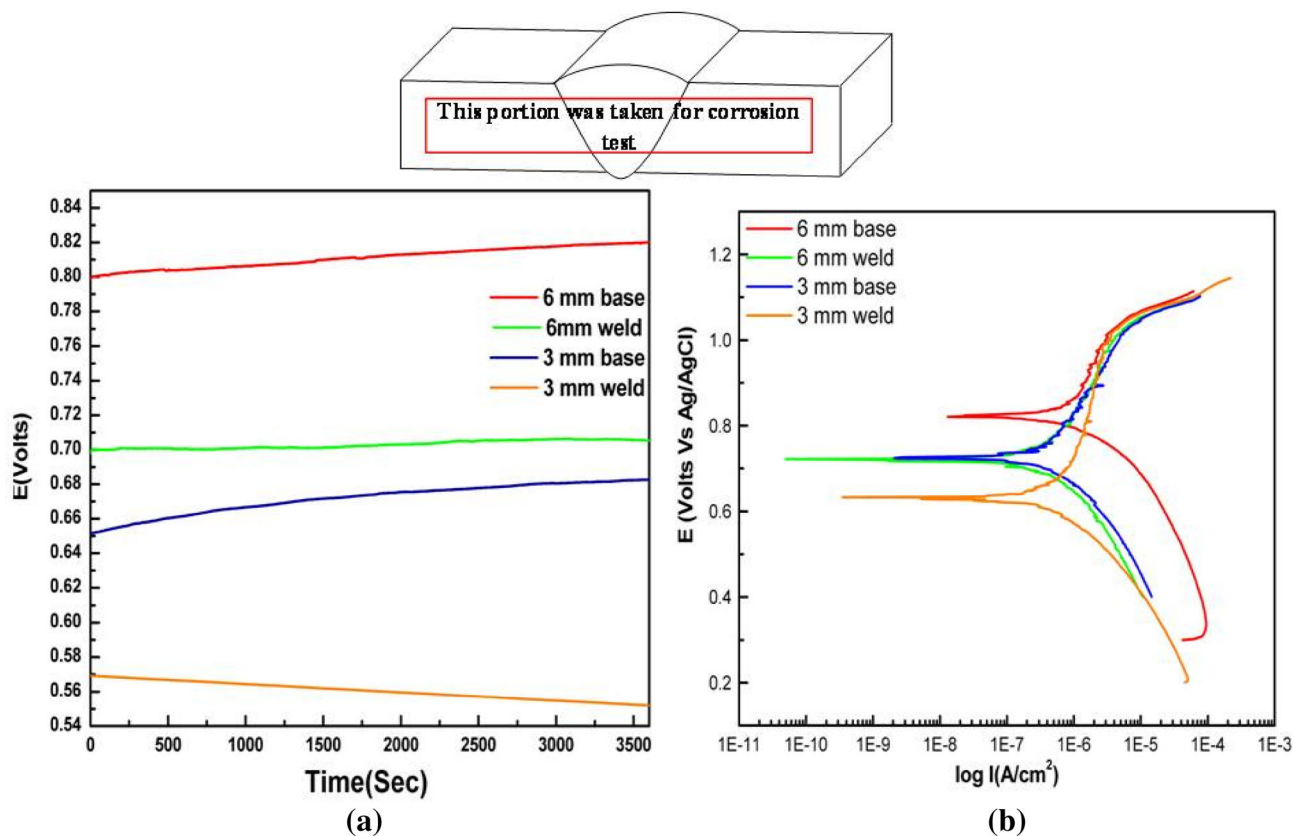
Fig. 12 **a** OCP and **b** potentiodynamic anodic polarization curve of type 304L stainless steel and its weldment of different thicknesses in 6 M HNO$_3$ solution

also be attributed to the role of Cr content and impurity/ alloying elements in grain boundaries that affect the IGC attack [5].

3.4 Electrochemical Corrosion Test Results

3.4.1 OCP Measurements

An electrochemical corrosion test has been performed in a 6 M nitric acid solution. The OCP and potentiodynamic anodic polarization measurement have been conducted to assess the corrosion behaviors of type 304L stainless steel. Figure 12a shows the OCP curve of the base material and its corresponding welded specimen. The OCP value of 6-mm-thick base metal is 0.80 V (vs. Ag/AgCl) with marginally higher OCP value in comparison with its welded counterpart where it is 0.70 V (vs. Ag/AgCl). Similarly, for 3-mm base metal, the OCP value is 0.65 V (vs. Ag/AgCl) and 0.57 V (vs. Ag/AgCl) for the same thickness of the welded material. During the OCP measurement, the formation of a passive layer of chromium oxide is always observed within short time after immersion. The nobler OCP value for 6-mm-thick base metal in comparison with its welded metal counterpart indicates that the weldment is

less prone to corrosion in the acid environment. Similarly in comparison to the 3 mm weld and 3 mm base material, later has more positive OCP value in comparison to its weld counterpart in the nitric acid medium. Moreover, the difference in the OCP value between base and weldment materials is marginal for both 3 mm and 6 mm thicknesses. Therefore, the tendency in the formation of the galvanic couple is negligible in both cases [39].

3.4.2 Potentiodynamic Anodic Polarization

Figure 12b shows the potentiodynamic polarization curve of the different thicknesses of type 304L SS base and its corresponding welded material. The shift of E$_{corr}$ value toward the noble direction is observed in 6-mm weld compared to base metal and 3-mm weld. The E$_{corr}$ value for 3 mm weld metal is 0.63 V (vs. Ag/AgCl) whereas for base material shift towards more noble direction, it is 0.73 V (vs. Ag/AgCl). For 6 mm base, it shows the highest E$_{corr}$ value of 0.82 V (vs. Ag/AgCl) and for its weldment, E$_{corr}$ value shifts to 0.73 V (vs. Ag/AgCl). Thereby, the shifts of E$_{corr}$ to more noble potentials in 6 mm weld are similar to the shift in OCP (Fig. 11a) as observed in both weld alloy steels. The noble potential shifts of OCP (Fig. 11a) and

E_{corr} (Fig. 12b) are related to the autocatalytic reduction of nitric acid and strong polarization associated with nitric acid where passive film stability is lower and high corrosion rates can result [2, 5, 8]. This also indicates that active component (oxidant) involves nitrate anions, which are well known to be strongly oxidizing as normally observed in stainless steel [61, 62]. Similarly, the shift of E_{corr} and OCP in nitric acid is undesirable, which may result in transpassive corrosion. Transpassive corrosion is a typical SS corrosion in nitric acid as observed in higher temperature and nitric acid concentrations. The corrosion potential is shifts near to transpassive region, and SS suffers severe IGC attack at around the grain boundaries even if the steels are not sensitized [36, 60].

Similarly, the i_{corr} values are in lower range and the observed i_{pass} (Table 3) of both the base and weld metals toward E_{TP} are low ($\sim$ 0.0106 A/m^2). The i_{pass} is a measure of the anodic dissolution at a certain potential in the passive region [63], and this value gives an indication of the resistance of the materials against corrosion in the particular environments. A lower i_{pass} indicates a high corrosion resistance of the material in the environment [61]. Hence, a lower i_{pass} in base 304L SS is an indication of an increase in corrosion resistance [61]. In addition, differences in i_{pass} between base and weld alloys in all the studied concentrations are not significant [61]. This behavior can be explained also by the nature of the passive film and its stability that are produced during the anodic dissolution of the corrosion process that enhances passivation, leading to the formation of stable Cr_2O_3 film and transpassive region (oxidation of Cr_2O_3 to Cr(VI)) and oxidation of solvent (water) [17, 61]. Similarly, Mirshekari et al. [4] also reported that δ-ferrite content and the number of passes influence the hardness and corrosion resistance of multipass GTAW welded 304L stainless steel in 1 M H_2SO_4 medium at 25 °C.

The main property of stainless steel is the formation of passive film. During welding, the compositional mismatch alters the stability of the passive film; hence, there is a change in corrosion properties. For 3-mm weld, the passive region starts early and passive current density is high in comparison with its base material and also same trend is

observed for 6-mm-thick weld and base material. For the 6-mm-thick base metal, the passive current density is lower in comparison with its weld metal, and it is close to the only base metal. For all materials, transpassive region is in a similar potential range. And the passive region range is much lower for 6-mm-thick base metal than that of its weld, and it is higher for 3-mm-thick weldment. Number of passes for 3-mm weld is lesser than that of 6-mm weld. As a result, the segregation of alloying elements occur during welding for 3-mm-thick material, whereas segregation may lead to removal or alloy homogenization in 6-mm-thick material associated with large number of passes. Segregation of element is the main issue in the ferrite phase, whereas it is most effective in the austenite phase of the steel [4].

3.4.3 Electrochemical Impedance Spectroscopy Measurements

The EIS measurements of Nyquist and Bode plots have been carried out for type 304L SS (base and weld) in 6 M nitric acid to study the electrochemical nature and passive film characteristics as shown in Fig. 13. In Fig. 13a, the Nyquist plots are characterized by a single semicircle arc for all the samples. This is also attributed to the nature of the passive film and charge transfer process at the metal/electrolyte interface [42].

From the Nyquist plot shown in Fig. 13a, it is evident that 3-mm weld has highest polarization resistance (R_p) value 0.0179 kΩ m^2 and the semicircle radius decreases from 3 mm weld to 3 mm base, and corresponding polarization resistance (R_p) value is 0.0129 kΩ m^2; for 6-mm-thick sample, polarization resistance (R_p) value is lesser than that of 3-mm-thick sample. Among the weld and base materials, 6-mm weld metal shows the higher value of resistance polarization (0.0094 kΩ m^2) than that of its corresponding base counterpart (0.0083 kΩ m^2). Therefore, the corrosion resistance of the 3-mm weld metal is higher than that of the base metal; 6-mm-weld metal shows higher corrosion resistance tendency than that of its base counterpart but lower corrosion resistance than that of 3-mm base metal.

The Bode plot measurement in 6 M nitric acid solution is shown in Fig. 13b. It is evident that the impedance magnitude varies with the frequency region associated with the nature of passive film formation. The magnitude of impedance in higher-frequency region is related to the oxidation process and depicts the anodic behavior of the sample, whereas the lower-frequency region is associated with the reduction behavior of the nitric acid. The double-layer capacitance (C_{dl}) is obtained by this relation [61–63]:

$$|z| = 1/C_{dl} \qquad (4)$$

Table 3 Corrosion parameters obtained from potentiodynamic polarization curve and by fitting Tafel plot

Samples	E_{corr} (V vs. Ag/AgCl)	i_{corr} (A/cm^2)	i_{pass} (A/cm^2)
6-mm base metal	0.82	1.45×10^{-6}	7.4×10^{-7}
6-mm weld	0.72	5.5×10^{-7}	2.3×10^{-7}
3-mm base metal	0.73	6.4×10^{-7}	3.3×10^{-7}
3-mm weld	0.63	2.9×10^{-7}	6.1×10^{-7}
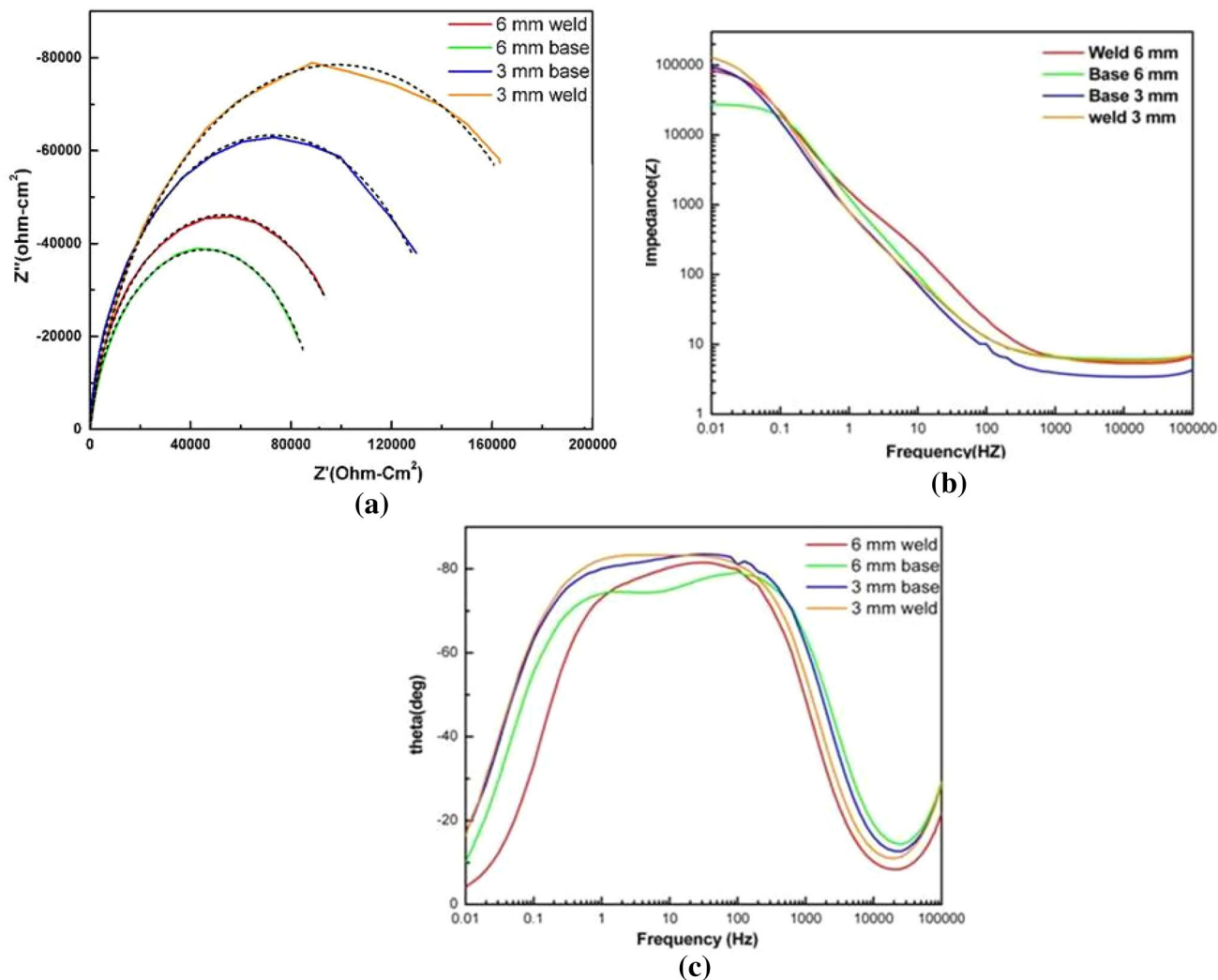
Fig. 13 EIS measurement of type 304L SS and its weldment of different thicknesses in 6 M HNO$_3$ solution **a** Nyquist plot, **b** Bode plot (impedance vs. frequency) and **c** Bode plot (phase angle vs. frequency)

The |z| is obtained from the slope of the intermediate straight line region. This double-layer capacitance value is necessary to estimate the thickness of the passive film and which is estimated by this relation [62].

$$l = \frac{\varepsilon \varepsilon_0}{C_{dl}} A \tag{5}$$

where l is the thickness of the passive film, ε is the dielectric constant of the passive film, by assuming pure oxide the value as 40; ε_0 is the vacuum permittivity, and its value is 8.85×10^{-12} F m^{-1}; A is effective surface area of the sample; and C_{dl} is the capacitance of the double-layer film [61].

The Bode plot shown in Fig. 13c reveals a variation of phase angle (theta) with frequency (Hz). A wide frequency range of 0.01–10^5 Hz measurement shows high phase angle value in 6 M nitric acid solution, which decreases from 3 mm weldment to 6 mm base metal. In 3-mm weld

metal, higher phase angle value of 83° and for 6-mm base metal a lower value of phase angle (79°) are observed, indicating that the passive film stability in 6 M nitric acid solution is higher for 3-mm weld compared to 6-mm base metal.

The equivalent circuit fitted with simple Randle cell is shown in Fig. 2, where the double-layer capacitance (C_{dl}) represents the CPE parallel to impedance, i.e., the resistance of polarization (R_p) and in series with solution resistance (R_s) [42, 64]. The fitted and calculated impedance parameters are enlisted in Tables 4 and 5. The 3-mm weld metal shows a lower value of CPE (1.14×10^{-9} F/m^{2}S^{-n}), whereas 6-mm base metal shows higher value (2.13×10^{-9} F/m^{2}S^{-n}). The lowest value of CPE corresponds to a thicker and more protective passive film that provides better resistance to corrosion [42, 62].

Table 4 EIS equivalent circuit fitting results of the system

Equivalent circuit element	Sample			
	6-mm base metal	6-mm weld	3-mm base metal	3-mm weld
Rs (KΩ m^2)	9.1×10^{-8}	9.2×10^{-8}	9.5×10^{-8}	9.7×10^{-8}
Rp (KΩ m^2)	0.0092	0.0082	0.0127	0.0178
CPE 1-T (F/m^{2}S^{-n})	2.13×10^{-1}	2.73×10^{-1}	1.85×10^{-1}	1.14×10^{-1}
CPE 1-P	0.92	0.92	0.94	0.97

Table 5 Details of the passive film properties obtained from EIS results in nitric acid

Sample	Double-layer capacitance ($C_{dl} = 1/|Z|$) (μF/m^2)	Thickness of the passive film $l = \frac{\varepsilon\varepsilon_0}{C_{dl}}A$ (Å)
6 mm weld	0.0001	3.67
6 mm base	0.0001	3.54
3 mm base	0.0093	3.80
3 mm weld	0.0093	7.15

4 Conclusions

In the present work, different thickness of GTAW welded 304L stainless steel of microstructure, hardness and corrosion resistance behavior have been evaluated. Based on the present experimental result, the following conclusion can be drawn:

1. All the welded samples showed an austenite microstructure with some amount of δ-ferrite. The δ-ferrite showed interdendritic features and decreased with thickness from 6 mm-weld to 3 mm weld metal. The lathy and skeletal features within austenite were also evident.

2. The microhardness value of the welded region near to the base metal region showed maximum value, attributed to the higher percentage of δ-ferrite present near to HAZ. The hardness value was maximum for 6-mm-thick welded sample.

3. The measured grain sizes were 40 μm and 22.2 μm for 6-mm and 3-mm base metals, and the corrosion rate of 6-mm-thick base material (11.42 mpy or 0.29 mm/y) was higher than that of 3-mm-thick base material (8.26 mpy or 0.21 mm/yr) attributing to the reduction in thickness affected by rolling of the samples.

4. The corrosion test was performed on the composite zone (fusion + HAZ + base), and marginally lower corrosion rate of the weldment material of 10.1 mpy or 0.26 mm/yr (6 mm) and 7.47 mpy or 0.19 mm/yr (3 mm) indicated that the delta ferrite contents with higher amount of chromium than that of the austenite matrix in the microstructure resulted in lower corrosion rate in the weldment compared to its base material as evident from the EDS/EDAX measurements.

5. Potentiodynamic anodic polarization and ASTM A-262 practice-C test (Huey test) revealed shift in corrosion potential value towards noble potential depending on the weld and base metal thickness. Further, a lower corrosion current density and passive current density in base metal of type 304L SS was an indication of an increase in corrosion resistance.

6. The EIS analysis from Nyquist and Bode plots showed that the polarization resistance value for 3-mm weld metal was larger ($R_p = 0.0177076$ kΩ m^2) than the 6-mm weld ($R_p = 0.0092581$ kΩ m^2) and correspondingly marginal variation in phase angle between base and welded metals were observed and could be attributed to the nature of passive film stability.

References

1. Karcı F, Kacar R, and Süleyman G, *J Mater Process Technol* **209** (2009) 4011.
2. Sedriks A J, *Corrosion of Stainless Steels*, Wiley (1979)
3. Raj B, and Mudali U K, *Prog Nucl Energy* **48** (2006) 283.
4. Mirshekari G R, Tavakoli E, Atapour M, and Sadeghian B, *Mater Des* **55** (2014) 905.
5. Ningshen S, and Sakairi M, *J Solid State Electrochem* **19** (2015) 3533.
6. Wang J, Xiong J, Peng Q, Fan H, Wang Y, Li G, and Shen B, *Mater Charact* **60** (2009) 197.
7. Verma J, and Taiwade R V, *J Manuf Process* **25** (2017) 152.
8. Dhas J E R, and Dhas J H, *Procedia Eng* **38** (2012) 544.
9. Grimma A, Schulzeb S, Silvaa A, Göbela G, Standfussa J, Brennera B, Beyera E, and Füsselb U, *Mater Today Proc* **2S** (2015) S169.

10. Shukla A K, Sharma V M J, Murty S V S N, Narayanan P R, and Sharma S C, *Procedia Eng* **86** (2014) 8.
11. Ibanez P, Chien S, Dinyavari M, Dobbs M, Gundy W, Howard G, Keowen R, Rentz P, Smith C, Stoessel J, Walton W, and Yifat C S, *Nucl Eng Des* **64** (1981) 1.
12. Eyre B L, *Prog Mater Sci* **42** (1997) 23.
13. Li H, Zou J, Yao J, and Peng H, *J Alloys Compd* **727** (2017) 531.
14. Boumerzoug Z, Derfouf C, and Baudin T, *Engineering* **2** (2010) 502.
15. Yeganeh V E, and Li P, *Mater Des* **124** (2017) 78.
16. Rao C V, Reddy G M, and Rao K S, Def Technol **11** (2015) 123.
17. Mehrpouya M, Gisario A, and Elahinia M, *J Manuf Process* **31** (2018) 162.
18. Wang G, Zhao Y, and Hao Y, *J Mater Sci Technol* **34** (2018) 73.
19. Ragunathan S, Balasubramanian V, Malarvizhi S, and Rao A G, *Def Technol* **11** (2015) 308.
20. Unnikrishnan R, Idury K S N S, Ismail T P, Bhadauria A, Shekhawat S K, Khatirkar R K, and Sapate S G, *Mater Charact* **93** (2014) 10.
21. Lee D J, Jung K H, Sung J H, Kim Y H, Lee K H, Park J U, Shin Y T, and Lee H W, *Mater Des* **30** (2009) 3269.
22. Yan J, Gao M, and Zeng X, *Opt Lasers Eng* **48** (2010) 512.
23. Pinnow K E, and Moskowitz A, *Weld J* **49** (1970) 278.
24. Colombier L and Hochmann J, *Stainless and Heat Resisting Steels New York*, St. Martin's Press (1968)
25. Nilsson J O, Karlsson L, and Andersson J O, *J Mater Sci Technol* **11** (1995) 276.
26. Atamert S, and King J E, *Acta Met Mater* **39** (1991) 273.
27. Sejč D I P, and Kubíček R, *Sci Proc* **19** (2011) 8.
28. Zumelzu E, Sepulveda J, and Barra M, *J Mater Process Technol* **94** (1999)36.
29. Baek J H, Kim Y P, Kim W S, and Kho Y T, *Int J Press Vessels Pip* **78** (2001) 351.
30. Messler R W Jr, *Principles of Welding*, John Wiley and Sons, USA (1999).
31. Mohammed G R, Ishak M, Aqida S N, and Abdulhadi H A, *IOP Conf Ser Mater Sci Eng* **257** (2017) 012072.
32. Kou S, *Welding Metallurgy* (2nd Edition), John Wiley& Sons, Inc., Hoboken (2003), p 17.
33. Korinko P S, and Malene S H, *Pract Fail Anal* **4** (2001) 61.
34. Raj B, Mudali U K, Jayakumar T, Kasiviswanathan K V, and Natarajan R, *Sadhana* **25** (2000) 519.
35. Balbaud F, Gerard S, Fauvet P, Santarini G, and Picard G *Corros Sci* **42** (2000) 1685
36. Ningshen S, Sakairi M, Suzuki K, and Ukai S, *Corros Sci* **78** (2014) 322.
37. Ningshen S, Mudali U K, Mukherjee P, Sarkar A, Barat P, Padhy N, and Raj B, *Corros Sci* **50** (2008) 2124.
38. Padhy N, Ningshen S, Panigrahi B K, and Mudali U K, *Corros Sci* **52** (2010) 104.
39. Ningshen S, Mudali U K, Amarendra G, and Raj B, *Corros Sci* **51** (2009) 322.
40. Drogowska M, Ménard H, Lasia A, and Brossard L, *J Appl Electrochem* **26** (1996) 1169.
41. Hsu C H, and Mansfeld F, *Corrosion* **57** (2001) 747.
42. Ningshen S, Kamachi U M, Ramya S, and Raj B, *Corros Sci* **53** (2011) 64.
43. Leone G L, and Kerr H W, *Weld J* **61** (1982) 13.
44. David S A, *Weld J* **59** (1980) 4.
45. Lippold J C, *Welding Metallurgy and Weldibilty*, John Wiley and Sons, Inc., Hoboken (2015)
46. Kou S, *Welding Metallurgy* (2nd edition) John Willey, USA (2003).
47. J F Lancaster, *Metallurgy of Welding* (6th edition), Abington Publishing, England (2009).
48. Little R, *Welding and Welding Technology* (1st edition), McGraw Hill (2001).
49. Welding Handbook (8th edition), volume 1 and 2, American Welding Society, USA (2007).
50. Gowrisankar I, Bhaduri A K, Seetharaman V, Verma D D N, and Achar D R G, *Weld J* **5** (1987) 147.
51. David S A, *Weld J* **4** (1981) 63.
52. Lippold J C, and Kotecki D J, *Welding Metallurgy and Weldibilty of Stainless Steel*, John Wiley and Sons, Inc., Canada (2005).
53. Das N M, Lotto A, Berretetta J R, and De R W, *Weld Int* **24** (2010) 739.
54. Kumar S, and Shahi A S, *Mater Des* **32** (2011) 3617.
55. Awang M, Raza S K, and Yahaya M S A, *J Mater Sci Eng Technol* **46** (2015) 492.
56. Musa M H A, Maleque M A, and Ali M Y, *IOP Conf Ser Mater Sci Eng* **290** (2018) 012041.
57. Shome M, *Mater Sci Eng A* **445–446** (2007) 460.
58. Schino A D, and Kenny J M, *J Mater Sci Lett* **21** (2002) 1631.
59. Dasgupta A, Karthikeyan T, Saroja S, Raju V R, Vijayalakshmi M, Dayal R K, and Raghunathan V S, *J Mater Eng Perform* **16** (2007) 800.
60. Fauvet P, Balbaud F, Robin R, Tran Q T, Mugnier A, and Espinoux D, *J Nucl Mater* **375** (2008) 52.
61. Ningshen S, Sakairi M, Suzuki K, and Okuno T, *Corros Sci* **91** (2015) 120.
62. Armstrong R D, and Cleland G E, *J Appl Electrochem* **28** (1998) 1205.
63. Ningshen S, and Mudali U K, *J Mater Eng Perform* **19** (2010) 274.
64. Olsson C O A, and Landolt D, *Electrochem Acta* **48** (2003) 1093.